Biosensors and Bioelectronics 207 (2022) 114176

Contents lists available at ScienceDirect

Biosensors and Bioelectronics

journal homepage: www.elsevier.com/locate/bios

Enhanced cathodic photocurrent derived from N-type S doped-Bi_2WO_6 nanoparticles through an antenna-like strategy for photoelectrochemical biosensor

Simin Ai, Yaling Liu, Yaqin Chai, Ruo Yuan, Hongyan Liu *

Key Laboratory of Luminescence Analysis and Molecular Sensing (Southwest University), Ministry of Education, College of Chemistry and Chemical Engineering, Southwest University, Chongqing, 400715, China

ARTICLE INFO

Keywords:
Antenna-like strategy
S doped-Bi_2WO_6
PEDOT
Self-powered
Cathodic photoelectrochemical
Biosensor

ABSTRACT

The sensitivity of cathodic photoelectrochemical (PEC) biosensor is mainly limited by the weak photocurrent response of p-type semiconductors due to the intrinsic weak hole conduction and severe charge recombination. Herein, we developed an antenna-like strategy that can amplify 10-fold of the cathodic photocurrent without using of p-type semiconductor. Specifically, poly (3,4-ethyl-enedioxythiophene) (PEDOT) was used as photocathode to improve the migration of photo-generated electrons (e^-) from the n-type S doped-Bi_2WO_6 ($Bi_2WO_{6-x}S_x$) photoanode through the external circuit and therefore an amplified cathodic photocurrent can be obtained toward such an antenna-like strategy. We further demonstrated that the antenna-like effect is originated from the super electrical conductivity of PEDOT photocathode and the facilitated charge separation of $Bi_2WO_{6-x}S_x$ photoanode by S doping. As a proof of concept, a self-powered dual-photoelectrode cathodic PEC biosensor driven by visible light was fabricated for microRNA-141 detection. Importantly, the biological recognition occurred at the photocathode could advance the anti-interference capability of the biosensor and show outstanding performance for microRNA-141 detection with a low limit of detection (LOD) of 0.3 fM. The antenna-like strategy offers a new method to amplify the cathodic photocurrent for sensitively PEC analysis.

1. Introduction

MicroRNAs (miRNAs) are confirmed as a kind of potential biomarkers of cancer (Chen et al., 2020). The rapid and sensitive detection of specific MicroRNAs is of vital importance in the fields of diagnosis of genetic diseases. Numerous analysis methods including electrochemistry (Zhang et al., 2018), electrochemiluminescence (Xu et al., 2017), fluorescence (Chang et al., 2021) and photoelectrochemistry (Zhao et al., 2021) have been proposed. Among these methods, the new emerged self-powered photoelectrochemical (PEC) sensing system has implemented considerable attention because of its simple instrumentation, excellent analytical performance, as well as low costs (Liu et al., 2020; Peng et al., 2021). It has been shown potential applications in the bio-analysis, food safety and environmental detection (Feng et al., 2021b; Yao et al., 2020). Basically, a cathodic self-powered photoelectrochemical biosensor is comprised of a photoanode and a photocathode. The photocathode based on p-type materials is used as a working electrode (WE) for the recognition of target and the photoanode based on n-type materials is used as a reference/counter electrode (RE/CE) to provide stable photocurrent as sensing signal, which can effectively prevent the nonspecific redox reaction of electroactivity interferences and avoid the false positive signals (Feng et al., 2021a; Yu et al., 2020). Various p-type semiconductors including NiO, PbS, Cu_2O, BiOI, and $CuInS_2$ are served as photocathode material (L. Li et al., 2020; Wang et al., 2021; Zhang et al., 2020). However, most of the p-type semiconductors based photocathode produce low photocurrent signal on account of the inescapable inherent weak hole conduction and severe charge recombination, which limits the sensitivity of the biosensors (Chen et al., 2019; Fan et al., 2016). Therefore, it is necessary but challenge to develop efficient strategy to enhance the charge separation efficiency and the conductivity of the photocathode.

Poly (3,4-ethyl-enedioxythiophene) (PEDOT), is a stable conducting polymer with colloidal processability and rich assembly behavior (Kim et al., 2020; Wu et al., 2021; Zheng et al., 2020). It has been widely explored in energy storage, organic light emitting diodes, photodecomposition and thermoelectric applications (Lee et al., 2016; Trzciński

* Corresponding author.
E-mail addresses: 2219086987@qq.com (S. Ai), liuhy860@swu.edu.cn (H. Liu).

https://doi.org/10.1016/j.bios.2022.114176
Received 9 January 2022; Received in revised form 11 February 2022; Accepted 7 March 2022
Available online 9 March 2022

et al., 2016). Based on the excellent conductivity and stable electrical behavior of PEDOT, it can be probably served as an alternative to increase the charge separation efficiency of the photocathode. Specifically, a PEDOT modified photocathode with excellent conductivity probably can improve the migration of photo-generated e^- from a n-type photoanode material through the external circuit. Therefore, the improved charge separation can significantly enhance the cathodic photocurrent through such an antenna-like strategy. To further fabricate high-performance cathodic PEC biosensor based on the above mentioned antenna-like strategy, the design of photoanode material is of vital importance. Many n-type semiconductors including metal oxides and metal sulfides are usually served as photoanode material (Ge et al., 2019, 2020). Among them, Bi_2WO_6 has attracted great attention because of its unique orthorhombic structure, consisting of alternating $(Bi_2O_2)_n^{2n+}$ layers and perovskite-like $(WO_4)_n^{2n-}$ layers (Zhang et al., 2020). Nevertheless, pristine Bi_2WO_6 suffers from the high recombination rate of electron-hole pairs. Great effort has been devoted to increase the photo-absorption and electron-hole separation efficiency. For example, noble metals such as silver and gold nanoparticles were deposited on Bi_2WO_6 material to improve the separation effect of carriers by surface plasma resonance (SPR) effect (Zhang et al., 2012). Moreover, heterojunctions such as Bi_2S_3/Bi_2WO_6 (Yi et al., 2019), Fe_2O_3/Bi_2WO_6 (Adhikari et al., 2019) and $CuInS_2/Bi_2WO_6$ (Luo et al., 2018) were fabricated to facilitate the charge separation. However, the construction of heterojunctions requires the matching of the energy band of photoactive materials and the interface between different materials increases the distance of electron transmission, which limits the photoelectric conversion efficiency (Ai et al., 2021; Zeng et al., 2021). Recent studies have demonstrated that doping can improve the photocatalytic activity of Bi_2WO_6 materials (Ding et al., 2014; Huang et al., 2014; Li et al., 2016). Non-metallic element S, as the same main group elements with O, is considered as efficient non-metal dopant. It was found that mixing the sulfur 3p states and oxygen 2p states contributed to the increase of the valence bandwidth, producing the defect states in the band gap of TiO_2 (Lin et al., 2016). Therefore, it is reasonable to suppose that doping of S can introduce defect states in Bi_2WO_6 materials, so as to enhance the separation of photo-generated carriers and further improve the photoelectric conversion efficiency of Bi_2WO_6.

Motivated by the above facts, in this work, a self-powered photocathodic biosensor based on antenna-like strategy was fabricated via using PEDOT as photocathode and S-doped Bi_2WO_6 ($Bi_2WO_{6-x}S_x$) as photoanode material. As shown in Scheme 1A, the $Bi_2WO_{6-x}S_x$ modified GCE as the photoanode was excited by visible light to generate e^- and h^+. The h^+ can be neutralized by H_2O_2 in the electrolyte to produce O_2, while photo-generated e^- can transfer to PEDOT photocathode through the external circuit and facilitate the capture of dissolved O_2 to obtain an amplified cathodic photocurrent. With the target microRNA-141 (miRNA-141) induced double-stranded specific nuclease (DSN) enzyme-assisted signal amplification process, the hairpin DNA 1 (HP1) on the Fe_3O_4–Au specifically blocked by Hexanethiol (HT), could be converted to large amount of output DNA (Scheme 1B). Subsequently, the capture probes (the hairpin 2, HP2) were immobilized on the PEDOT photocathode as a sensing electrode as displayed in Scheme 1C. The output DNA could open the HP2. After the adding of HP3 and S1 modified SiO_2 NPs (HP3–S1–SiO_2) and S2 modified SiO_2 NPs (S2–SiO_2), HP2 could hybridize with HP3 to form a double-stranded DNA through the chain displacement. During this process, the output DNA was released to open other HP2 on the electrode. Meanwhile, S2 could hybridize with S1 to form a DNA-SiO_2 nanocluster on the electrode surface. The photocurrent signal could be significantly reduced because of the low conductivity and steric hindrance of SiO_2. The changes of the photocurrent signal are associated with the concentration of the target miRNA-141. The photocathodic biosensor based on antenna-like effect demonstrates a fresh strategy to improve the performance of PEC biosensors for sensitively detecting various biomarkers.

2. Experimental section

2.1. Preparation process of $Bi_2WO_{6-x}S_x$ and PEDOT solution

The $Bi_2WO_{6-x}S_x$ materials were prepared according to a modified version of a previously reported procedure for synthesis of Bi_2WO_6 (Huo et al., 2019). Typically, 0.9701 g $Bi(NO_3)_3{\cdot}5H_2O$ dissolved in 20 mL glycol was magnetically stirred for 30 min to acquire solution A. Meanwhile, solution B was obtained by dissolving 0.3297 g $Na_2WO_4{\cdot}2H_2O$ into 20 mL glycol under magnetically stirring for 30 min. Then, solution B was added into solution An under continuous agitation, followed by adding thiourea as the sulfur source. The mass ratio of thiourea to Bi_2WO_6 was 0, 1%, 3%, 5%, 10%, respectively. After stirring for 1 h, the solution was transferred to a polytetrafluoroethylene lined autoclave and reacted at 180 °C for 24 h. The resulted gray precipitates were washed using ethanol and water and freeze-dried overnight. In

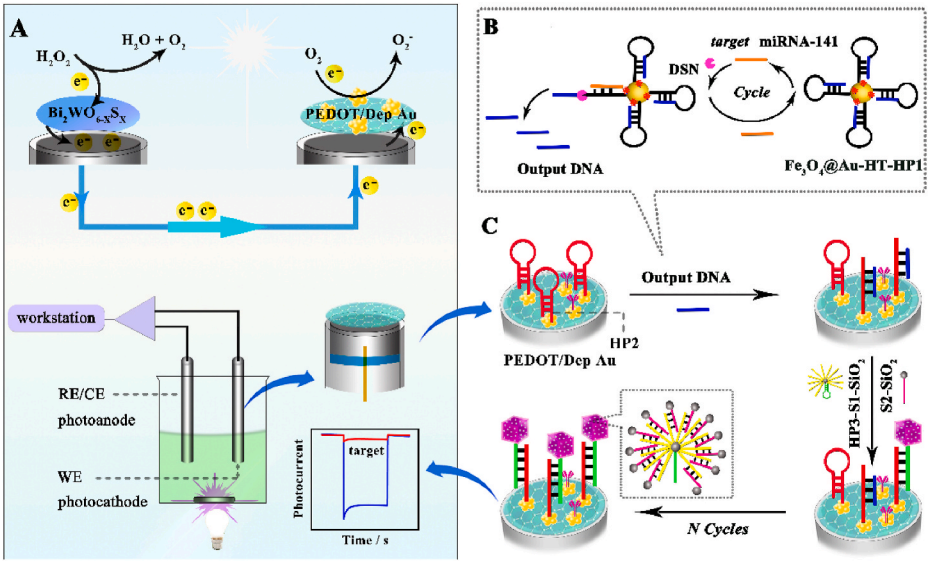

Scheme 1. Schematic illustration of (A) the electron transfer mechanism of self-powered dual-photoelectrode cathodic PEC biosensor (PEDOT/dep Au photocathode as the working electrode (WE), $Bi_2WO_{6-x}S_x$ photoanode as the reference/counter electrode (RE/CE)); (B) the target-induced double-stranded specific nuclease (DSN) enzyme-assisted dual signal amplification process; (C) the fabrication of the photocathode biosensor.

addition, Poly (3,4-ethyl-enedioxythiophene) (PEDOT) was prepared by a reported method (Chiu et al., 2005). Firstly, a mixed solution was obtained via adding dropwise 3,4-Ethylenedioxythiophene (EDOT, 0.20 g) to aqueous ammonium persulfate solution (20 ml, 0.31 M) and keeping stirring for 72 h. Secondly, the prepared black precipitations were centrifuged and washed with water, followed by removal of unreacted oligomers and monomers with methanol (20 ml) and acetone (3 ml). Finally, the products were dried with a freeze dryer.

2.2. Double-stranded specific nuclease (DSN) enzyme-assisted signal amplification for detection of miRNA-141

As depicted in Scheme 1B, Fe_3O_4-Au-HP1 was prepared by adding 120 μL hairpin DNA 1 (HP1) (2 μmol/L) into the Fe_3O_4–Au solution (480 μL) under stirring overnight at 4 °C. Subsequently, the mixture was magnetically separated, washed and redistributed into 120 μL phosphate buffer solution (PBS, 0.1 M, pH = 7.4). Hexanethiol (HT) was added to block the non-specific binding sites on the magnetic beads in Fe_3O_4-Au-HP1 complex. Then, 20 μL target miRNA-141, 0.5 μL of DSN (0.1 U) and 0.5 μL 1 × DSN master buffer were added to 20 μL Fe_3O_4-Au-HP1-HT complex and kept reaction for 40 min at 60 °C. During this process, the target miRNA-141 can hybridize with HP1 on Fe_3O_4–Au to form DNA-RNA hybrid chain. DSN enzyme can specifically recognize and digest the DNA part of DNA-RNA hybrid chain, so as to release RNA for the next cycle, the output DNA was also released. DSN stop solution (2 μL) was then added to denature the DSN and the output DNA was obtained by magnetic separation.

2.3. Fabrication of the self-powered cathodic PEC biosensor

The self-powered cathodic PEC biosensor was fabricated on the bare glassy carbon electrode (GCE), which was burnished with alumina powder and washed with ethanol and ultrapure water three times respectively. Firstly, for the photoanode, 10 μL $Bi_2WO_{6-x}S_x$ (2 mg/mL) was immobilized on the GCE to provide the photocurrent signal. Secondly, for cathodic PEC biosensor, as displayed in Scheme 1C, 10 μL 1 mg/mL PEDOT was dropped on the surface of GCE, followed by electrodeposition in $HAuCl_4$ (1%) solution for 15 s at −0.2 V to obtain PEDOT/dep Au photocathode. The construction of the aforementioned two-electrode system can obtain stronger initial cathode photocurrent signal under the optimal experimental conditions (Fig. S1). Then, 10 μL 2 μmol/L HP2 solution was added dropwise to the PEDOT/dep Au photocathode for incubation at 4 °C for 12 h 10 μL 0.1 mmol/L HT was then added to the electrode and incubated for 40 min for blocking the non-specific sites. After that, 10 μL output DNA was dropped on the above prepared photocathode and incubated at 37 °C for 2 h. Finally, 10 μL HP3–S1–SiO_2 complex and 10 μL S2–SiO_2 complex (preparation process provided by the supplementary material) were added onto the photocathode for 2 h at 37 °C. HP2 can hybridize with HP3, and S1 can hybridize with S2, releasing the output DNA to open other HP2.

3. Results and discussion

3.1. Characterization of the $Bi_2WO_{6-x}S_x$ and PEDOT materials

The morphology of the synthesized $Bi_2WO_{6-x}S_x$ material was characterized by transmission electron microscopy (TEM). As shown in Fig. 1A–B, $Bi_2WO_{6-x}S_x$ sample is evenly dispersed with uniform size and an irregular rod structure. High-resolution TEM indicates that the interplanar distances of the lattice fringes are 0.315 nm and 0.830 nm, corresponding to the (131) and (020) planes of Bi_2WO_6, respectively (Fig. 1C). Elemental mappings of $Bi_2WO_{6-x}S_x$ (Fig. 1D) show the homogeneously distribution of Bi, O, W and S elements. Moreover, the energy dispersive X-ray (EDX) spectroscopy of the $Bi_2WO_{6-x}S_x$ also indicates the doping of S in the sample (Fig. S2). The crystal structure of $Bi_2WO_{6-x}S_x$ was analyzed by X-ray diffraction (XRD). Fig. 1E depicts that the peaks at 28.4°, 32.9°, 47.1°, 56.0° and 58.6° are correspond to the (131), (002), (202), (331) and (262) crystal planes of the rhombic Bi_2WO_6 (JCPDS NO.39-0256), suggesting that the doping of S did not change the lattice structure of Bi_2WO_6. The chemical state of the $Bi_2WO_{6-x}S_x$ was then investigated by X-ray photoelectron spectroscopy (XPS). Fig. 1F shows the XPS surveys of Bi_2WO_6 and $Bi_2WO_{6-x}S_x$ sample. The characteristic peaks of Bi, W, and O are observed both in the Bi_2WO_6 and $Bi_2WO_{6-x}S_x$ sample. The high resolution XPS characterizations of Bi

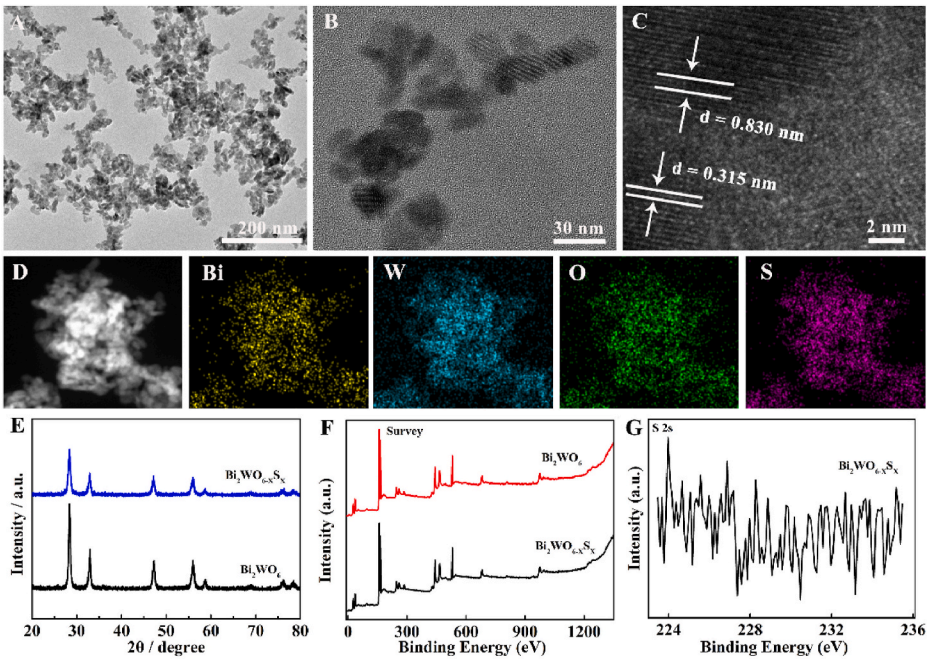

Fig. 1. (A, B) Transmission electron microscopy (TEM) image of $Bi_2WO_{6-x}S_x$. (C) High-resolution transmission electron microscopy (HRTEM) of $Bi_2WO_{6-x}S_x$. (D) The element mappings of Bi, O, W and S of $Bi_2WO_{6-x}S_x$ sample. (E) X-ray diffraction (XRD) patterns of Bi_2WO_6 and $Bi_2WO_{6-x}S_x$. (F) Survey X-ray photoelectron spectroscopy (XPS) spectrum of Bi_2WO_6 and $Bi_2WO_{6-x}S_x$. (G) High-resolution XPS spectrum of S 2s of $Bi_2WO_{6-x}S_x$.

4f and W 4f reveal that the valence state of Bi and W were +3 and + 6, respectively (Fig. S3). As displayed in Fig. 1G, the characteristic peak of S 2s was very weak, probably because of the low percentage of S. The pristine PEDOT displays an amorphous structure without clearly definite morphology (Fig. S4).

3.2. Photoelectric properties of $Bi_2WO_{6-x}S_x$ material and the mechanism study

The photoelectrochemical performance of the $Bi_2WO_{6-x}S_x$ material was firstly evaluated by instantaneous photocurrent measurement in the traditional three-photoelectrode system. As shown in Fig. 2A, $Bi_2WO_{6-x}S_x$ shows a notably higher photocurrent intensity (4.998 μM) under visible-light (400 nm) than pristine Bi_2WO_6, indicating the doping of S can probably facilitate electrons and holes separation. For further exploring the enhancement mechanism, the electron-transfer efficiency was then detected by electrochemical impedance spectra (EIS) measurement. The $Bi_2WO_{6-x}S_x$ sample exhibits a lower charge-transfer resistance than Bi_2WO_6 (Fig. 2B), suggesting that the charged-defects could facilitate the separation and transport of photo-generated carriers. Moreover, the energy levels of the $Bi_2WO_{6-x}S_x$ sample were characterized by the valence band (VB) XPS and UV–vis diffuse reflectance spectra (DRS). As shown in Fig. 2C, the VB maximums of $Bi_2WO_{6-x}S_x$ and Bi_2WO_6 are 1.96 eV and 2.18 eV, respectively. The Eg values of $Bi_2WO_{6-x}S_x$ and Bi_2WO_6 acquired from the Tauc plot (Fig. S5) are 2.57 and 2.29 eV, respectively. Therefore, it can be calculated that the conduction band (CB) values of $Bi_2WO_{6-x}S_x$ and Bi_2WO_6 are −0.61 eV and −0.11 eV, respectively. Compared with Bi_2WO_6, the band potential of $Bi_2WO_{6-x}S_x$ is more negative than Bi_2WO_6, which results in improved PEC performance due to the fast charge separating facilitation (Adhikari and Kim, 2018). The photoluminescence (PL) spectra could effectively reflect the generation and separation of photogenerated carriers. As shown in Fig. S6, $Bi_2WO_{6-x}S_x$ shows a lower PL emission intensity than Bi_2WO_6, showing that the recombination rate of the photogenerated electron-hole pairs can be effectively suppressed by S-doping. All of the above results demonstrate that doping sulfur can change effectively enhance the charge separation to improve the photoelectric performance. $Bi_2WO_{6-x}S_x$ materials with different ratios of S doping were then prepared to optimize the PEC performance. As shown in Fig. S7, the highest photocurrent signal is obtained when the mass ratios of S to Bi_2WO_6 is 1%. The photocurrent signal decreases when the concentrations of S are 5% and 10%, indicating that the defects in high content supplying recombination sites for electrons and holes. Therefore, the $Bi_2WO_{6-x}S_x$ with 1% S doping was used for the further construction of biosensor.

3.3. Design principle of the self-powered photocathodic biosensor

As presented in Fig. 3A, a self-powered dual-photoelectrode cathodic PEC biosensor was fabricated under intermittent visible light excitation, which comprised of PEDOT photocathode with excellent conductivity and $Bi_2WO_{6-x}S_x$ photoanode with ultrasensitive visible-light-responsive properties. The detailed illustration for an in-depth understanding of the principle of enhanced cathodic photocurrent was also proposed. $Bi_2WO_{6-x}S_x$ is excited by visible light (400 nm) to generate e^- and hole (h^+) pairs contemporaneously. Holes in the VB of GCE/$Bi_2WO_{6-x}S_x$ are neutralized by H_2O_2 to produce O_2, while the migration of relevant e^- in the CB are rapidly improved by PEDOT photocathode through the external circuit due to the excellent electrical conductivity of PEDOT. In addition, the e^- transfer to the Au NPs rapidly and then can be trapped by the dissolved O_2 which acted as an electron acceptor to produce $\bullet O_2^-$. Ultimately, an amplified cathodic photocurrent can be obtained toward such an antenna-like strategy.

3.4. PEC and CV characterization of the constructed biosensor

PEC and cyclic voltammetry (CV) measurements were employed to characterize the stepwise fabrication process of the self-power PEC biosensor. As shown in Fig. 3B, the weak cathodic photocurrent signal is −0.474 μA (curve a) when using $Bi_2WO_{6-x}S_x$ as the photoanode and bare GCE as the photocathode. Surprisingly, curve b shows a remarkable cathodic photocurrent when PEDOT was immobilized on the GCE as

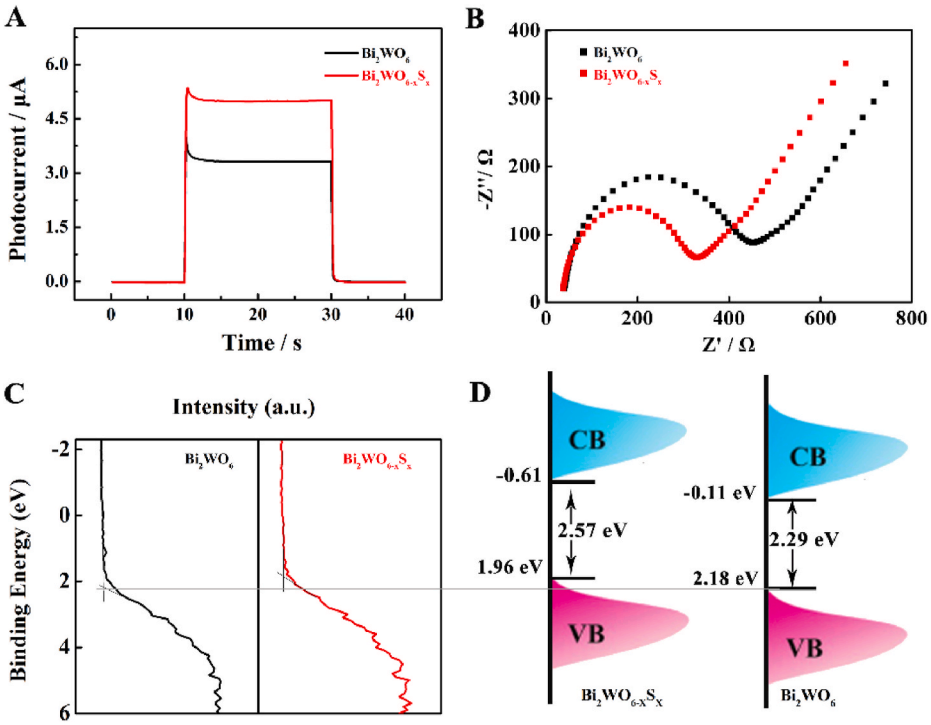

Fig. 2. The photoanode current response excited by 400 nm visible-light ($Bi_2WO_{6-x}S_x$ as the WE, saturated calomel electrode as the RE, Pt electrode as the CE) (A), EIS spectra (B), valence-band XPS spectra (C) and band structure graph (D) of Bi_2WO_6 and $Bi_2WO_{6-x}S_x$.

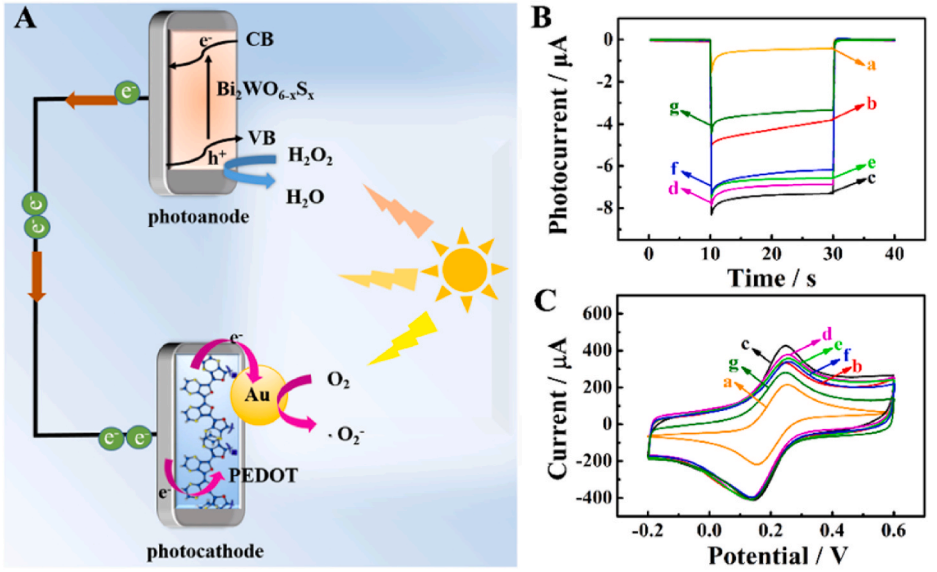

Fig. 3. The design principle of the self-powered photocathodic biosensor (A); The photocurrent response under visible-light (400 nm) (PEDOT/dep Au as the photocathode, $Bi_2WO_{6-x}S_x$ as the photoanode) (B) and CV responses (C) of photocathode with different modified layer: (a) bare GCE, (b) GCE/PEDOT, (c) GCE/PEDOT/dep Au, (d) GCE/PEDOT/dep Au/HP2, (e) GCE/PEDOT/dep Au/HP2/HT, (f) GCE/PEDOT/dep Au/HP2/HT/output DNA, and (g) GCE/PEDOT/dep Au/HP2/HT/output DNA/HP3–S1–SiO_2/S2–SiO_2.

photocathode (I = −4.271 μA), suggesting the high photoelectric conversion efficiency of $Bi_2WO_{6-x}S_x$ and the excellent conductivity of PEDOT can significantly enhance the cathodic photocurrent through such an antenna-like strategy. After depositing Au NPs on the PEDOT photocathode, the photocathodic current was further increased owing to the conductivity of Au NPs (curve c). Moreover, the photocurrent decreased after the modification of DNA HP2 and the blocking agent HT (curve d, e). The cathodic photocurrent decreased obviously after the successively incubation of the output DNA, HP3–S1–SiO_2 and S2–SiO_2 composite due to the presence of large amount of SiO_2 nanoparticles with poor conductivity (curve f, g). Furthermore, the construction process of PEC sensing platform was represented by cyclic voltammetry (CV). As exhibited in Fig. 3C, there was an obvious redox peaks of bare GCE (curve a). The redox peak current was significantly increased when PEDOT was modified on the electrode (curve b) and increased significantly after the deposition of Au NPs (curve c), owing to the excellent electroconductivity of the PEDOT and Au NPs. Finally, with the continuous assembly of HP2, HT, output DNA, HP3–S1–SiO_2 complex and S2–SiO_2 complex, it could be observed that the peak current is decreased (curve d-g).

3.5. Analytical performance of the PEC biosensor

To evaluate the analytical performance of the proposed cathodic PEC

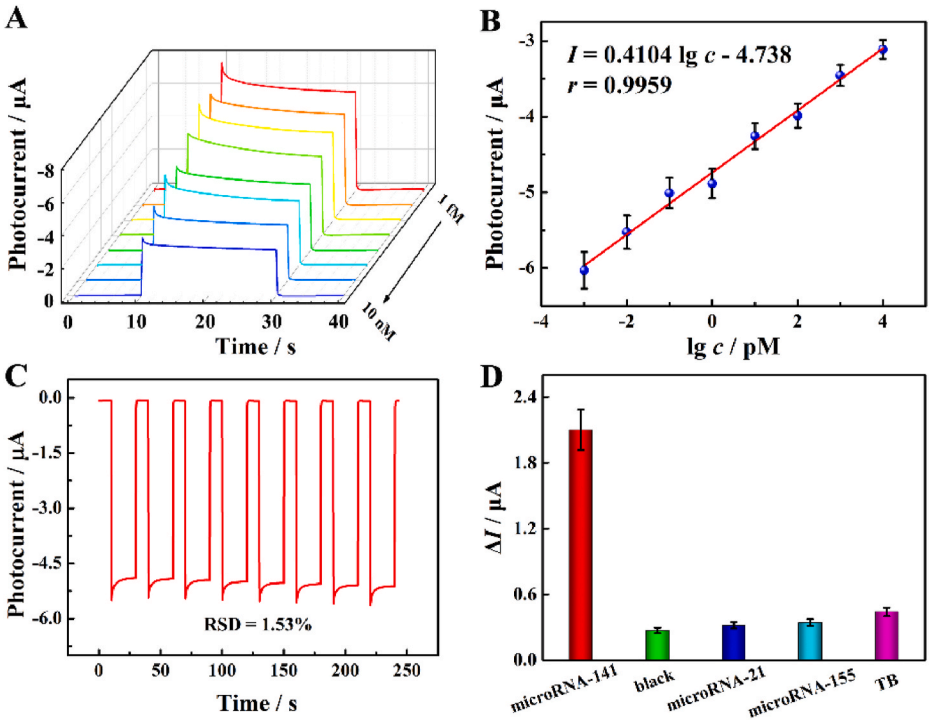

Fig. 4. (A) Photocurrent intensity of the cathodic PEC biosensor at a wavelength of 400 nm for miRNA-141 with various concentrations from 1 fmol/L to 10 nmol/L. (B) Calibration curve between photoelectric signals and the logarithm of miRNA-141 concentrations. (C) Stability of the cathodic PEC biosensor under consecutive off-on-off light for 8 cycles. (D) Selectivity of the cathodic PEC for the interferences (100 pmol/L): the blank, microRNA-21, microRNA-155 and TB.

biosensor, the photocurrent signal of the target miRNA-141 with various concentrations was monitored under the optimal experimental conditions (Fig. S1). Fig. 4A and B shows the linear relationship as monitored by the PEC signal versus the logarithm of the miRNA-141concentration. It can be seen that the cathodic photocurrent decreases with the increasing miRNA-141 concentration. The obtained linear equation was $I = 0.4104 \lg c - 4.738$ ($r = 0.9959$). The detection limit was estimated to be 0.3 fM (S/N = 3), which was lower than those of previous reported miRNA-141 biosensor (Table 1), indicating the photocathodic biosensor possessed eminent analytical performance for ultra-sensitive detection of miRNA-141.

3.6. Stability, reproducibility and selectivity of the proposed PEC biosensor

In order to explore the stability of the fabricated cathodic PEC biosensor, the photocathodic signals was scanned for 8 cycles under consecutive "off–on–off" light. As shown in Fig. 4C, there is unconspicuous changes in 1 pM miRNA-141 and the relative standard deviation (RSD) value is 1.53%, indicating the high excellent stability of the biosensor. In addition, the reproducibility was investigated with RSD of four electrodes incubated in the intra-assay and inter-assay under the same experimental condition (the concentration of miRNA-141 was 1 pM). As depicted in Fig. S8, there are no apparent differences in photocathodic signals and the RSD values were assessed to be 1.12% and 1.54%, respectively, illustrating the excellent reproducibility of the biosensor. Simultaneously, the selectivity of the PEC biosensor to miRNA-141 was investigated by using microRNA-21, microRNA-155 and thrombin (TB) as the interfering substances. As shown in Fig. 4D, an obviously decrease of photocurrent (2.102 μA) is observed for 10 pM miRNA-141. In comparison, there is no significant change of the photocurrent when the concentration of interference is 100 pM. The results indicate that the cathodic PEC biosensor exhibits good selectivity and reproducibility for miRNA-141 detection.

3.7. Detection of miRNA-141 in clinical serum samples

The sensing performance for miRNA-141 extracted from human real serum samples (the Ninth People's Hospital of Chongqing, China) was investigated to preliminarily estimate its feasibility and application. Various concentrations of microRNA-141 were respectively added into 50-fold-diluted serum samples. Table S2 exhibits the recoveries are between 91.40% and 108.7%. The RSDs ranges from 2.3% to 7.8%, demonstrating the fabricated PEC biosensor possessed potential applicability in clinic researches and biomedical analysis.

4. Conclusions

In summary, a self-powered dual-photoelectrode cathodic PEC biosensor based on an antenna-like strategy was ingeniously fabricated by using n-type S-doped Bi_2WO_6 ($Bi_2WO_{6-x}S_x$) as photoanode and conductive polymer PEDOT as photocathode without external voltage. It was demonstrated that PEDOT with distinguished conductivity probably can improve the migration of the photo-generated e^- from the $Bi_2WO_{6-x}S_x$ photoanode through the external circuit. Therefore, drastically amplified cathodic photocurrent was obtained toward an antenna-like strategy. The high performance photocathode boosted the anti-interference capability and sensitivity of the self-powered PEC biosensor, with LOD of 0.3 fM. This work not only provided a strategy to amplify the cathodic photocurrent for fabrication of highly sensitive PEC sensing platforms, but also showed great application potential in accurate diagnosis of diseases.

CRediT authorship contribution statement

Simin Ai: Conceptualization, Data curation, Formal analysis, Writing – original draft, Writing – review & editing. **Yaling Liu:** Software, Data curation, Writing – review & editing. **Yaqin Chai:** Conceptualization, Supervision. **Ruo Yuan:** Conceptualization, Supervision. **Hongyan Liu:** Writing – review & editing, Funding acquisition, Supervision.

Table 1
Comparison of the performance of different methods for miRNA-141 detection.

Detection technology	Detection range	Detection limit	Reference
Fluorescent	100 pM–100 nM	44.9 pM	Chang et al. (2021)
Chemiluminescence	10 fM ~ 50 pM	3.02 fM	Ling et al. (2018)
Electrochemiluminescence	10 fM ~ 100 pM	3.3 fM	Xu et al. (2017)
PEC	1 pM ~ 50 nM	0.2 pM	Zhao et al. (2021)
PEC	350 fM ~ 5 nM	153 fM	Tu et al. (2016)
PEC	2 fM ~ 170 pM	0.6 fM	Li et al. (2020)
PEC	1 fM ~ 10 nM	0.3 fM	this work

Declaration of competing interest

The authors declare that they have no conflicts of interest to this work. We declare that we do not have any commercial or associative interest that represents a conflict of interest in connection with the work submitted.

Acknowledgements

This work was financially supported by the Chongqing Research Program of Basic Research and Frontier Technology (cstc2020jcyj-msxmX0386) and the National Natural Science Foundation of China (21501081).

Appendix A. Supplementary data

Supplementary data to this article can be found online at https://doi.org/10.1016/j.bios.2022.114176.

References

Adhikari, S., Kim, D.-H., 2018. Chem. Eng. J. 354, 692–705.
Adhikari, S., Selvaraj, S., Kim, D.-H., 2019. Appl. Catal. B Environ. 244, 11–24.
Ai, S.M., Zeng, H.M., Chai, Y.Q., Yuan, R., Liu, H.Y., 2021. Sensor. Actuator. B Chem. 340, 129942.
Chang, W.-H., Lee, Y.-F., Liu, Y.-W., Willner, I., Liao, W.-C., 2021. Nanoscale 13, 16799–16808.
Chen, K., Huang, Q., Fu, T., Ke, G.L., Zhao, Z.L., Zhang, X.B., Tan, W.H., 2020. Anal. Chem. 92, 7404–7408.
Chen, Y.X., Ji, W.H., Yan, K., Gao, J., Zhang, J.D., 2019. Nano Energy 61, 173–193.
Chiu, W.W., Travaš-Sejdić, J., Cooney, R.P., Bowmaker, G.A., 2005. Synth. Met. 155, 80–88.
Ding, X., Zhao, K., Zhang, L.Z., 2014. Environ. Sci. Technol. 48, 5823–5831.
Fan, G.-C., Shi, X.-M., Zhang, J.-R., Zhu, J.-J., 2016. Anal. Chem. 88, 10352–10356.
Feng, J.H., Dai, L., Ren, X., Ma, H.M., Wang, X.Y., Fan, D.W., Wei, Q., Wu, R.D., 2021a. Anal. Chem. 93, 7125–7132.
Feng, J.H., Wu, T.T., Cheng, Q., Ma, H.M., Ren, X., Wang, X.Y., Lee, J.Y., Wei, Q., Ju, H. X., 2021b. Lab Chip 21, 378–384.
Ge, L., Hong, Q., Li, H., Li, F., 2019. Chem. Commun. 55, 4945–4948.
Ge, X.X., Zhou, P., Zhang, Q.H., Xia, Z.H., Chen, S.L., Gao, P., Zhang, Z., Gu, L., Guo, S.J., 2020. Angew. Chem. Int. Ed. 59, 232–236.
Huang, H.W., Liu, K., Chen, K., Zhang, Y.L., Zhang, Y.H., Wang, S.C., 2014. J. Phys. Chem. C 118, 14379–14387.
Huo, W.C., Dong, X.A., Li, J.Y., Liu, M., Liu, X.Y., Zhang, Y.X., Dong, F., 2019. Chem. Eng. J. 361, 129–138.
Kim, J.I., Zhang, X.B., Pascuzzi, P.E., Liu, C.-J., Chapple, C., 2020. New Phytol. 225, 154–168.
Lee, H.J., Anoop, G., Lee, H.J., Kim, C., Park, J.-W., Choi, J., Kim, H., Kim, Y.-J., Lee, E., Lee, S.-G., Kim, Y.-M., Lee, J.-H., Jo, J.Y., 2016. Energy Environ. Sci. 9, 2806.
Li, C.M., Chen, G., Sun, J.X., Rao, J.C., Han, Z.H., Hu, Y.D., Xing, W.N., Zhang, C.M., 2016. Appl. Catal. B Environ. 188, 39–47.
Li, L., Zhang, Y., Zhao, Y., Chen, M.Q., Zhang, L.N., Zhao, P.N., Yu, J.H., 2020. ACS Sens. 5, 1482–1490.

Li, Y.W., Liu, L., Feng, J.H., Ren, X., Zhang, Y., Yan, T., Liu, X.J., Wei, Q., 2020. Biosens. Bioelectron. 154, 112089.
Lin, Y.-H., Hsueh, H.-T., Chang, C.-W., Chu, H., 2016. Appl. Catal. B Environ. 199, 1–10.
Ling, K., Jiang, H.Y., Huang, X., Li, Y., Lin, J.J., Li, F.-R., 2018. Chem. Commun. 54, 1909–1912.
Liu, N.N., Qiao, H., Xu, K., Xi, Y.L., Ren, L., Cheng, N.Y., Cui, D.D., Qi, X., Xu, X., Hao, W. C., Dou, S.X., Du, Y., 2020. Small 16 (23), 2000283.
Luo, S., Ke, J., Yuan, M.Q., Zhang, Q., Xie, P., Deng, L.D., Wang, S.B., 2018. Appl. Catal. B Environ. 221, 215–222.
Peng, B., Lu, Y., Luo, J., Zhang, Z.L., Zhu, X., Tang, L., Wang, L.L., Deng, Y.C., Ouyang, X. L., Tan, J.S., Wang, J.J., 2021. J. Hazard Mater. 401, 123395.
Trzciński, K., Szkoda, M., Siuzdak, K., Sawczak, M., Lisowska-Oleksiak, A., 2016. Appl. Surf. Sci. 388, 753–761.
Tu, W.W., Cao, H.J., Zhang, L., Bao, J.C., Liu, X.H., Dai, Z.H., 2016. Anal. Chem. 88, 10459–10465.
Wang, H.Y., Qi, Y.T., Wu, D., Wei, Q., 2021. J. Hazard Mater. 416, 126201.
Wu, P.P., Wei, C.R., Yang, W.J., Lin, L.N., Pei, W.H., Wang, J.X., Jiang, L., 2021. ACS Appl. Mater. Interfaces 13, 41220–41230.
Xu, Z.Q., Liao, L.L., Chai, Y.Q., Wang, H.J., Yuan, R., 2017. Anal. Chem. 89, 8282–8287.
Yao, X.L., Gao, J., Yan, K., Chen, Y.X., Zhang, J.D., 2020. Anal. Chem. 92, 8026–8030.
Yi, W.J., Cai, R.L., Xiang, D.F., Wang, Y.X., Zhang, M.S., Ma, Q.H., Cui, Y.H., Bian, X.W., 2019. Biosens. Bioelectron. 143, 111614.
Yu, P., Wei, H., Zhong, P.P., Xue, Y.F., Wu, F., Liu, Y., Fei, J.J., Mao, L.Q., 2020. Angew. Chem. Int. Ed. 59, 22652–22658.
Zeng, H.M., Ai, S.M., Chai, Y.Q., Yuan, R., Liu, H.Y., 2021. J. Mater. Chem. C 9 7384–7391.
Zhang, B.H., Wang, H., Xi, J.J., Zhao, F.Q., Zeng, B.Z., 2020. ACS Sens. 5, 2876–2884.
Zhang, M.M., Wang, J.J., Xue, H., Zhang, J.F., Peng, S.J., Han, X.P., Deng, Y.D., Hu, W.B., 2020. Angew. Chem. Int. Ed. 59, 18463–18467.
Zhang, X.L., Yang, Z.H., Chang, Y.Y., Qing, M., Yuan, R., Chai, Y.Q., 2018. Anal. Chem. 90, 9538–9544.
Zhang, Z.J., Wang, W.Z., Gao, E.P., Sun, S.M., Zhang, L., 2012. J. Phys. Chem. C 49, 25898–25903.
Zhao, J.G., Fu, C.P., Huang, C., Zhang, S.B., Wang, F.F., Zhang, Y., Zhang, L.N., Ge, S.G., Yu, J.H., 2021. Chem. Eng. J. 406, 126892.
Zheng, H.J., Zhang, S., Liu, X.Q., Zhou, Y.M., Alwarappan, S., 2020. Biosens. Bioelectron. 162, 112234.